Journal of Power Sources 347 (2017) 29–36

Contents lists available at ScienceDirect

Journal of Power Sources

journal homepage: www.elsevier.com/locate/jpowsour

A simple route to improve rate performance of $LiFePO_4$/reduced graphene oxide composite cathode by adding Mg^{2+} via mechanical mixing

Yuan Huang [a, 1], Hao Liu [a, b, 1], Li Gong [c], Yanglong Hou [d], Quan Li [a, *]

[a] *Department of Physics, The Chinese University of Hong Kong, Shatin, New Territory, Hong Kong*
[b] *School of Science, China University of Geosciences (Beijing), Beijing, PR China*
[c] *Instrumental Analysis & Research Center, Sun Yat-sen University, Guangzhou, 510275, PR China*
[d] *Department of Materials Science and Engineering, College of Engineering, Peking University, Beijing, PR China*

HIGHLIGHTS

- Adding Mg^{2+} alone into LFP results in little improvement of rate performance.
- Introducing rGO to LFP results in moderately increased capacity at high rate.
- Adding Mg^{2+} into LFP/rGO cathode brings significantly improved rate performance.
- Enhanced reduction of Fe^{2+} to Fe^0 occurs in simultaneous presence of Mg^{2+} and rGO.

GRAPHICAL ABSTRACT

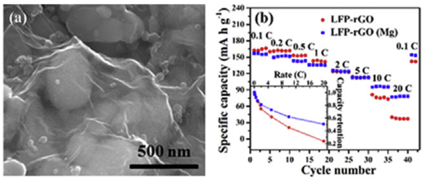

ARTICLE INFO

Article history:
Received 4 September 2016
Received in revised form
8 February 2017
Accepted 12 February 2017
Available online 20 February 2017

Keywords:
Mg^{2+}
Reduced graphene oxide
$LiFePO_4$
Li-ion battery
Rate performance

ABSTRACT

Introducing Mg^{2+} to $LiFePO_4$ and reduced graphene oxide composite via mechanical mixing and annealing leads to largely improved rate performance of the cathode (e.g. ~78 mA h g^{-1} at 20 C for $LiFePO_4$ and reduced graphene oxide composite with Mg^{2+} introduction vs. ~37 mA h g^{-1} at 20 C for $LiFePO_4$ and reduced graphene oxide composite). X-ray photoelectron spectroscopy unravels that the enhanced reduction of Fe^{2+} to Fe^0 occurs in the simultaneous presence of Mg^{2+} and reduced graphene oxide, which is beneficial for the rate capability of cathode. The simple fabrication process provides a simple and effective means to improve the rate performance of the $LiFePO_4$ and reduced graphene oxide composite cathode.

1. Introduction

$LiFePO_4$ (LFP) is one of the most promising cathode materials for lithium ion batteries (LIBs), due to its abundant material supply with its high theoretical capacity (170 mA h g^{-1}), low cost, good environmental compatibility, and excellent safety [1–3]. Nevertheless, it suffers from low rate capability mainly due to its low electronic conductivity [2–5].

Many attempts have been made to tackle this problem, including conductive surface coating on LFP particles [4], cation

---

* Corresponding author.
E-mail address: liquan@phy.cuhk.edu.hk (Q. Li).

[1] These authors have equally contributed.

http://dx.doi.org/10.1016/j.jpowsour.2017.02.043
0378-7753/

doping of LFP [6–8], reduction of LFP size [9], and addition of conductive additive into the electrode [10], etc. Introducing conductive materials to the LFP cathode has been commonly employed in preparing the LFP based cathode. Among various choices of conductive materials, graphene based materials are the most promising. Reduced graphene oxide (rGO) is cheap and easy to process with LFP to form composite electrode by mechanical mixing [10], hydrothermal reaction [11] or electrophoresis [12]. The LFP/rGO electrodes indeed exhibit superior rate capability to those of the conventional LFP electrodes (e.g., ~82 mA h g^{-1} at 10 C for LFP/rGO composite vs. ~60 mA h g^{-1} at 10 C for conventional LFP electrodes [12]). On the other hand, doping of Mg^{2+} into the LFP lattice has also been found to be beneficial for the rate capability of the LFP cathode [7]. It has been theoretically suggested that Mg^{2+} taking the substitutional site of Fe^{2+} in LFP can effectively improve the electronic conduction and ionic conductivity of the LFP [13]. Experimentally, improved electronic and ionic transport properties of LFP crystals has been found in Mg^{2+} doped mesoporous carbon-coated LFP nanocrystals, in which the Mg^{2+} doping is suggested by X-ray diffraction (XRD) and Rietveld refinement data [7].

In the present work, we show that introducing Mg^{2+} and rGO to LFP together via simple mechanical mixing and annealing leads to largely improved rate performance of the cathode, while adding Mg^{2+} or rGO alone results in little, or moderate performance (specific capacity) improvement of the same cathode, respectively. We discover that the additional improvement on rate performance of the LFP cathode (with Mg^{2+} and rGO) results from the enhanced reduction of Fe^{2+} to Fe^0 in the simultaneous presence of Mg^{2+} and rGO, rather than having Mg^{2+} doped into the LFP lattice. Our work provides a simple method that effectively improves the rate performance of the LFP/rGO cathode without disturbing the growth process of the active materials.

2. Experimental

2.1. Preparation of the LFP (Mg), LFP-rGO, LFP-rGO (Mg) composite

The commercial LFP powders (Advanced Lithium Electrochemistry Co., Ltd., Taiwan) were employed for the preparation of cathode electrode. LFP was dispersed in isopropyl alcohol (IPA) by sonication for 3 h, followed by adding $Mg(NO_3)_2 \cdot 6H_2O$ (LFP/Mg mass ratio 130/1). After drying, the powders were collected and annealed at 700 °C for 1 h under H_2 (volume 10%)/Ar atmosphere. The annealed LFP powders without adding $Mg(NO_3)_2 \cdot 6H_2O$ were also prepared following the same procedure for comparison.

The graphene oxide (GO) was prepared using the modified Hummers method [14]. The LFP powders and GO were dispersed in IPA by sonication for 3 h, respectively. Then they were mixed, followed by adding different amount of $Mg(NO_3)_2 \cdot 6H_2O$. The mixture was stirred for 1 h after 1hr ultrasonic dispersion. After drying, the composite were collected and annealed at 700 °C for 1 h under H_2 (volume 10%)/Ar atmosphere. The LFP/rGO composite without adding $Mg(NO_3)_2 \cdot 6H_2O$ was also prepared following the same procedure for comparison.

2.2. Structure and morphology characterization

The morphologies and compositions of the samples were characterized by a field emission scanning electron microscope (FESEM, Quanta 200, FEI). Transmission electron microscopy (TEM) was also carried out for more detailed structure analysis using a Tecnai F20 (FEI) microscope operating at 200 kV. The crystallinity and phases of the samples were examined by XRD (SmartLab, Rigaku) with a Cu-Ka radiation source ($d = 0.1541$ nm). Raman analysis was performed using a Micro Raman spectrometer (RM-1000, Renishaw Co., Ltd.) with a 10 mW helium/neon laser at 514 nm. X-ray photoelectron spectroscopy (XPS, Thermo Fisher Scientific ESCALAB 250) with a monochromatic Al Kα radiation source was used to investigate the elemental composition of composite and its binding state. The binding energy scale of the instrument was calibrated using Ar peak (242.1 eV). Thermal gravimetric analysis (TGA, Perkin-Elmer) was employed to quantify the amount of rGO in the LFP/rGO composite.

2.3. Electrochemical characterization

The electrochemical properties of the LFP/rGO composite were characterized by using CR2032 coin-type cells with Li foil as a counter electrode. The liquid electrolyte was 1.0 M $LiPF_6$ in the mixture of 1:1 (by volume) ethylene carbonate and diethyl carbonate (Novolyte Co.). The final cell was composed of 87 wt% LFP/rGO powder with Mg^{2+} (including 7 wt% rGO, total amount of LFP and Mg kept at ~80 wt%), 3 wt% acetylene black, and 10 wt% of polyvinylidene fluoride (PVDF) binder pasted on carbon cloth. As a comparison, conventional cells, consisting of 80 wt% annealed LFP powder or LFP (Mg), 10 wt% acetylene black, and 10 wt% of PVDF binder pasted on carbon cloth were prepared. Galvanostatic charging/discharging cycles were tested between 2.5 and 4.2 V vs. Li^+/Li at different rates on a multichannel battery test system (CT2001A, Wuhan Kingnuo Electronic Co., Ltd.). The electrochemical impedance spectroscopy (EIS) of the batteries was tested in the frequency range from 100 kHz to 2 Hz under an alternating current (AC) stimulus with a 5 mV of amplitude (CHI 660C, Shanghai Chenhua Instrument Co., Ltd.).

3. Results and discussions

3.1. Structure characterizations and electrochemical properties of LFP and LFP (Mg) sample

We first compare the LFP sample with or without Mg^{2+} introduction. rGO is not introduced to such samples. Commercial LFP powder with (LFP/Mg mass ratio of 130/1) or without Mg^{2+} is annealed before it is made into electrode. The two samples are denoted as LFP and LFP (Mg), respectively. The general morphology and crystal structure of the two samples are similar, and here we show the results of a representative one, i.e. LFP (Mg). The characterization of LFP is shown in Fig. S1 (Supporting Information).

The morphology of the LFP (Mg) powder is examined by SEM (Fig. 1(a)). The size of quasi-spherical particles ranges from 50 to 700 nm (with an average size of ~273 nm, Fig. 1(b)). Its crystallinity is examined using XRD and the result is shown in Fig. 1(c). All Bragg peaks can be indexed to the orthorhombic LFP phase. No additional peak or peak shifting is observed. Detailed structural characterization of the LFP (Mg) sample is carried out using TEM. High resolution TEM image taken from the surface region of LFP particle (Fig. 1(d)) discloses an amorphous carbon layer of ~3–4 nm coated on the LFP surface. The spatial distribution of the compositional elements is revealed by EDX elemental mapping (Fig. 1(e)–(k)), showing rather uniform distribution of the compositional elements.

The effect of adding Mg^{2+} on the electronic structure of LFP crystals is investigated by XPS. Fig. 2(a)–(c) compare the typical O 1s, P 2p, and Fe 2p spectra of LFP and LFP (Mg) samples. Fitting of the O 1s XPS spectra (Fig. 2(a)) shows peaks located at around 530.65, 531.50, and 532.60 eV, which are attributed to chemical shifts from Fe-O, P-O, and adsorbed OH^- [15]. The P 2p spectra in Fig. 2(b) shows single peak located at 133.2 eV, which is attributed to P^{5+} state resulting from the PO_4^{3-} group [16]. It can be seen that the Fe 2p spectra is split into $2p_{3/2}$ at ~710.0 eV and $2p_{1/2}$ at

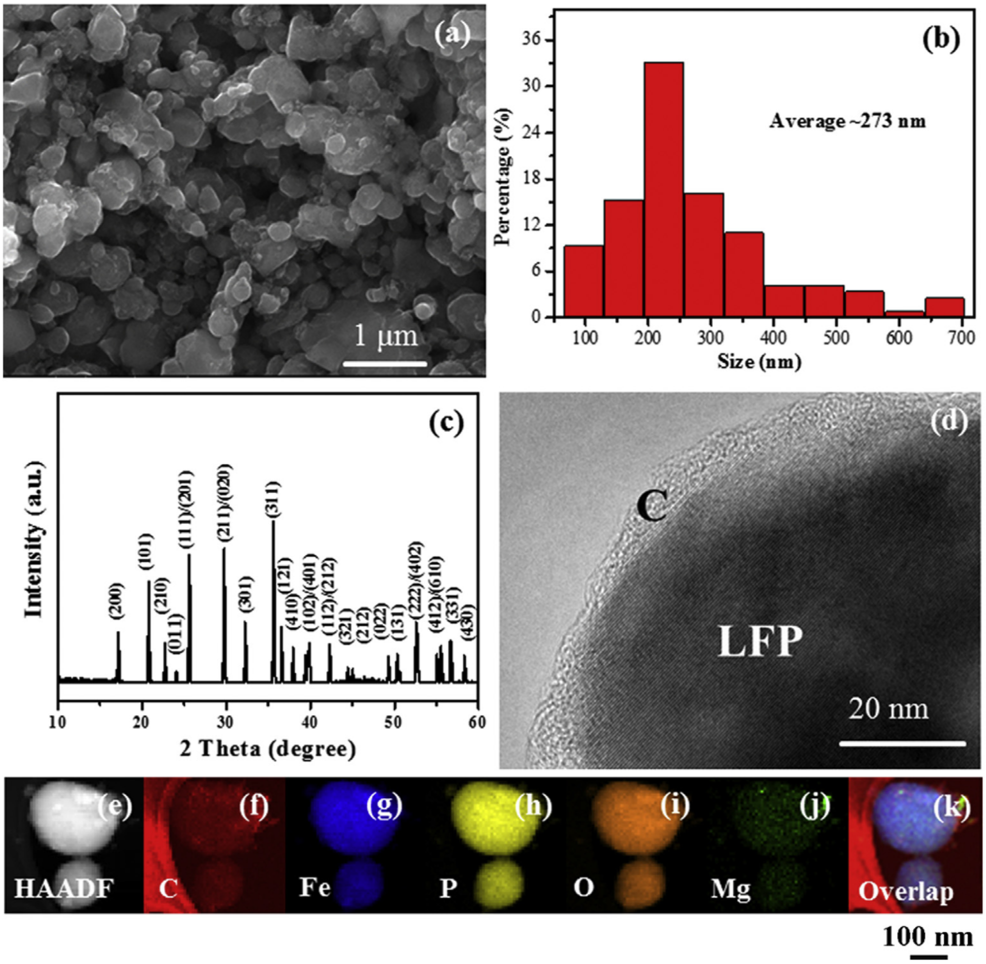

Fig. 1. (a) SEM image of the LFP (Mg) powder. (b) The size distribution of LFP (Mg) nanoparticles. (c) XRD spectrum of LFP (Mg) powder. (d) High resolution TEM image taken from the surface region of LFP (Mg) particle. (e) High angle annular dark field (HAADF) image taken from LFP (Mg) sample. (f)–(j) EDX elemental mapping taken from the same region shown in Fig. 1(e). (f) C; (g) Fe; (h) P; (i) O; and (j) Mg maps. (k) Overlap image of C, Fe, and Mg (The carbon signal in the left of Fig. 1(f) and (k) originates from the carbon support film).

~723.5 eV as a result of spin-orbit coupling [17]. The Fe $2p_{1/2}$ peak rides on a larger background [18], we therefore focus our discussion on Fe $2p_{3/2.}$ Fitting of the Fe $2p_{3/2}$ shows that it consists of a small peak at 706.8 eV, a main peak at 709.9 eV, and a broad signals at 714.0 eV. The peak at 706.8 eV is a characteristic peak of iron metal (Fe^0) [19]. The formation of metallic iron usually results from a reduction by the carbon (carbothermal reduction) during the annealing [20]. The area ratios of Fe^0 are estimated to be ~1.9% and ~2.0% in the Fe $2p_{3/2}$ spectra of LFP and LFP (Mg), respectively. The main peak of 709.9 eV is related to the valence of Fe^{2+} state in the LFP [21]. The broad signal at 714.0 eV corresponds to satellite signals [22]. Compared to LFP, no obvious change in the O 1s, P 2p, and Fe 2p spectra is detected in LFP (Mg), suggesting the little electronic structure change of LFP after the Mg^{2+} introduction. The Mg 1s spectrum of LFP (Mg) is shown in Fig. S2 (Supporting Information). The presence of peak at 1304 eV is characteristic of the Mg 1s core level (Mg^{2+}) [23].

Coin cells are assembled using the respective samples to evaluate effect of Mg^{2+} on the electrochemical performance of the electrode. Fig. 3(a) shows the first charging and discharging profiles of LFP and LFP (Mg) samples cycled at 0.1 C. The average plateau is observed around 3.42 V vs. Li^+/Li, corresponding to the reversible redox reaction between Fe^{2+}/Fe^{3+} in LFP particles. The polarization between the charging and discharging plateau for the LFP sample is ~76 mV, close to that of the LFP (Mg) sample (~78 mV). This indicates that the presence of Mg^{2+} in the sample does not significantly change the internal resistance of the electrodes. In addition, the LFP electrode shows a discharging capacity (normalized to the mass of LFP) of 156.8 mA h g^{-1} at 0.1 C rate, which is slightly higher than that of the LFP (Mg) sample (151.3 mA h g^{-1}). To further evaluate the electrochemical performance of the electrodes, these cells are tested under various charging/discharging rates and their specific capacities are shown in Fig. 3(b). Again, very similar rate performance is observed for the two samples. The capacity retention of the two samples (inset in Fig. 3(b)) is also similar. For example, at high charging/discharging rates of 20 C, the discharging capacities of the LFP (Mg) sample are maintained at ~32 mA h g^{-1}, corresponding to ~21% capacity retention of the first discharging capacity at 0.1 C. The LFP sample delivers the discharging capacities of ~30 mA h g^{-1} at 20 C, corresponding ~19% capacity retention of the first discharging capacity at 0.1 C. Good cycling performances of both the LFP and LFP (Mg) samples (tested at a rate of 10 C) are observed (Fig. 3(c)).

EIS is employed to find out the electrode impedance associated with the two samples. The measurements are carried out after charging the samples to ~4.2 V vs. Li^+/Li and their corresponding Nyquist plots are shown in Fig. 3(d). For a typical Nyquist plot of LIBs, the intercept impedance on the Z_{real} axis represents the ohmic

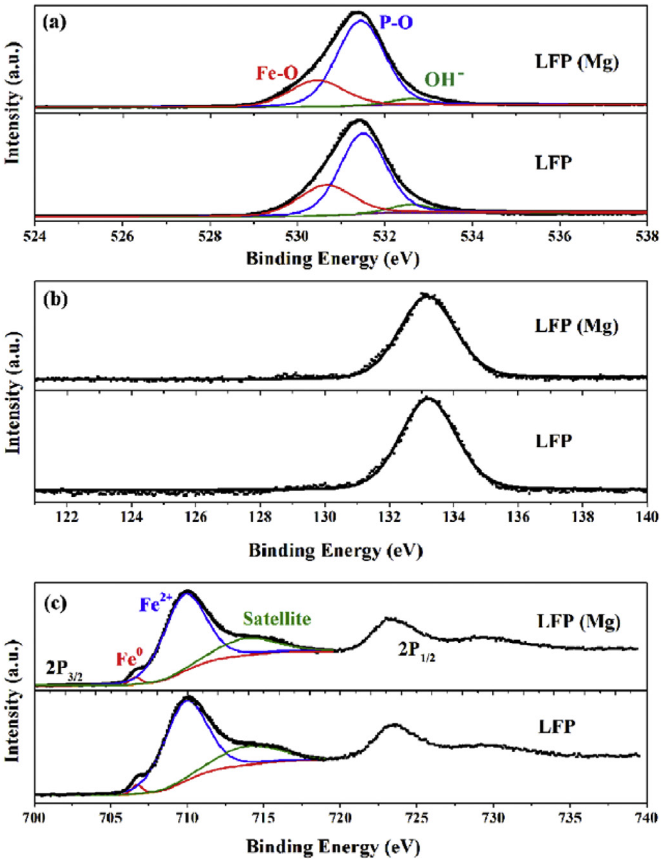

Fig. 2. (a) O 1s, (b) P 2p, and (c) Fe 2p XPS spectra of LFP and LFP (Mg).

resistance (R_{ser}), which is contributed by external cell connections and ionic conduction through the electrolyte and separator. The depressed semicircles at high and medium frequency region correspond to the resistance of the SEI layer (R_{sur}) and the resistance of the charge transfer (R_{ct}) on the electrode/electrolyte interface, respectively. The inclined line at 45° in low frequency region represents the diffusion of Li^+ in the solid-state electrode, which is also named as Warburg impedance [24]. An appropriate equivalent circuit model (inset in Fig. 3(d)) is established to fit the Nyquist curves. The electrical parameters (e.g., R_{ser}, R_{sur}, and R_{ct}) in this model can be calculated, as shown in Table S1 (Supporting Information). The estimated values of R_{ser}, R_{sur}, and R_{ct} for LFP are 4.7, 13.0, and 24.3 Ω, which are close to those for LFP (Mg) (R_{ser}, 6.6 Ω; R_{sur}, 12.1 Ω; R_{ct}, 26.6 Ω). The estimated values of the D_{Li} are ~1.79×10^{-10} and ~1.07×10^{-10} $cm^2\ s^{-1}$ for the LFP and LFP (Mg) samples, respectively. These results suggest that the presence of Mg^{2+} in the LFP sample leads to little change of its electrochemical properties, being consistent with the structural characterization results obtained from the two samples.

3.2. Structure characterizations and electrochemical properties of LFP-rGO and LFP-rGO (Mg)

The composite samples are obtained by mechanical mixing of LFP and GO with (LFP/Mg mass ratio of 130/1) or without a small amount of Mg^{2+}, followed by annealing at the same condition as the previous samples of LFP and LFP (Mg). We denote the two samples here as LFP-rGO and LFP-rGO (Mg), respectively. The morphological and the structural characteristics of the two samples are similar, and the only difference is the absence of Mg signal in the EDX measurement of the LFP-rGO sample (Fig. S3(a), Supporting Information).

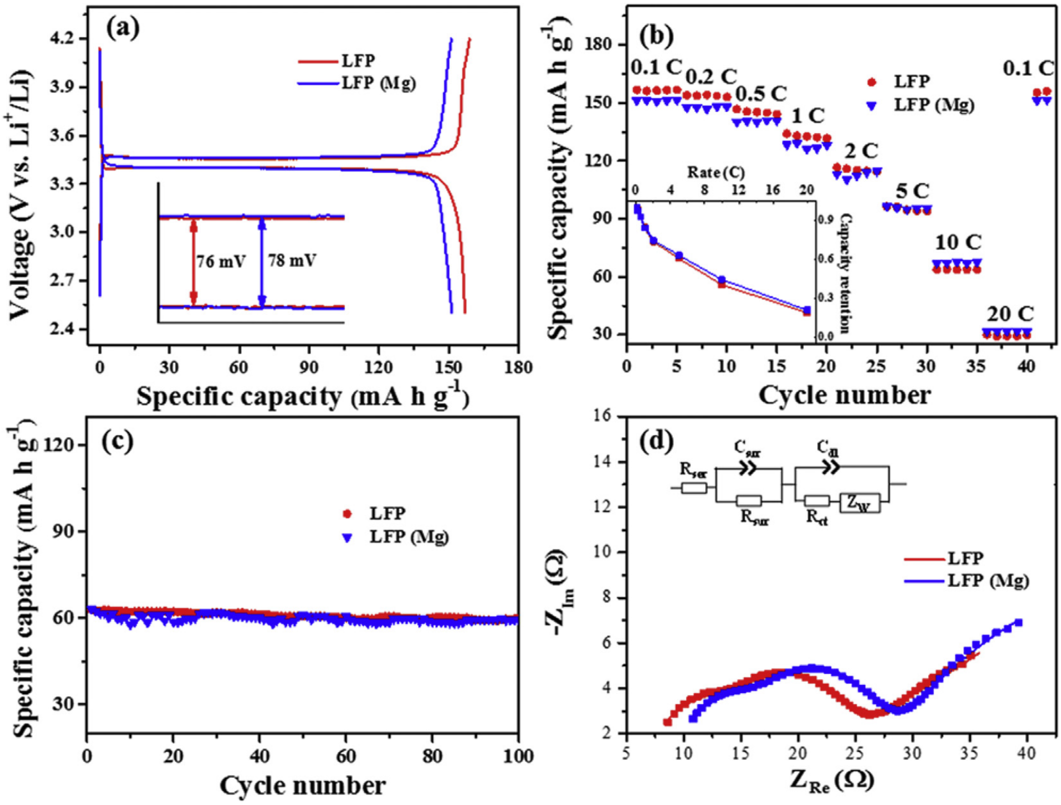

Fig. 3. (a) Comparison of the first charging and discharging profiles of LFP and LFP (Mg) at 0.1 C. (b) Specific capacities of the samples at various rates. (c) Cycling stability of the samples cycled at a rate of 10 C. (d) Nyquist plots of the electrodes after charging the samples to ~4.2 V vs. Li^+/Li.

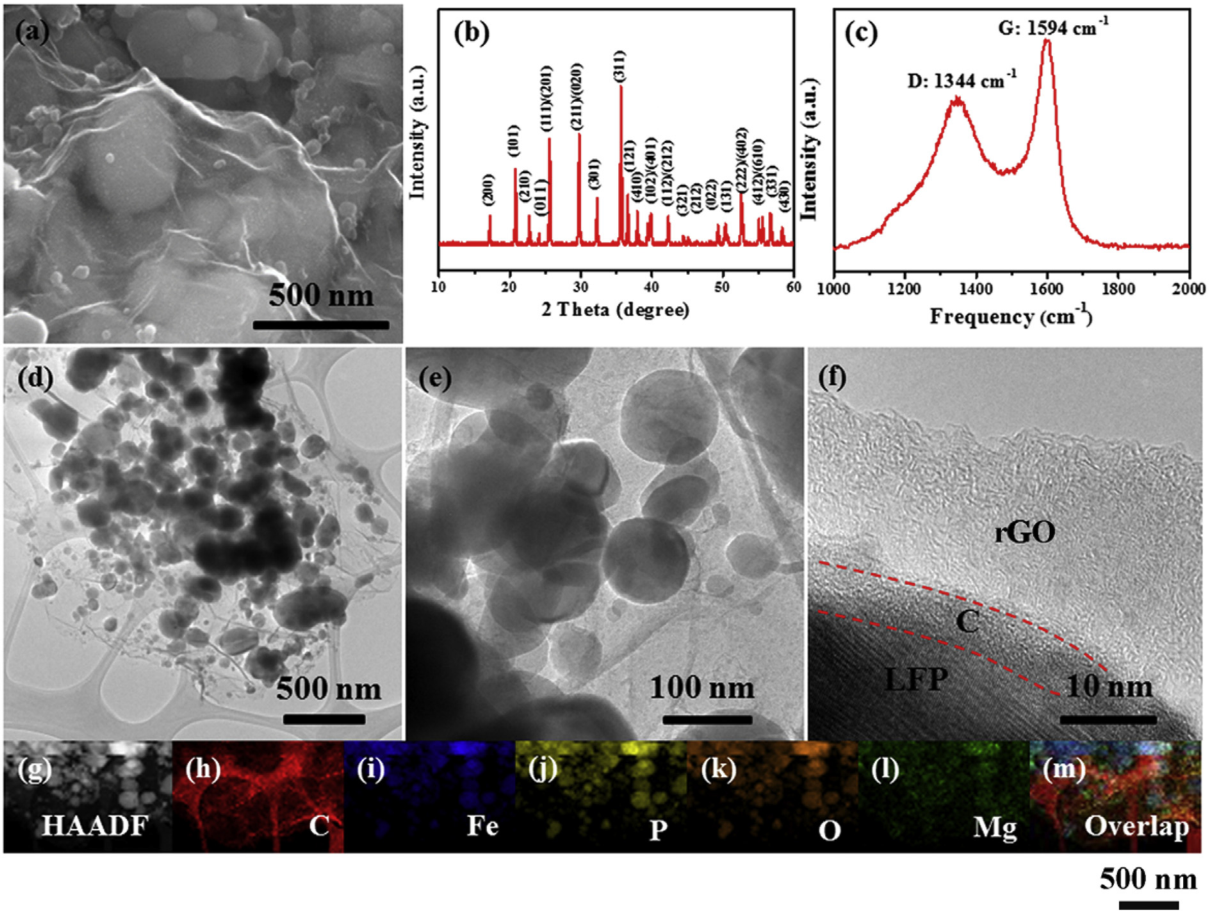

Fig. 4. (a) SEM image of the LFP-rGO (Mg) composite powder. (b) XRD spectrum of the LFP-rGO (Mg) composite. (c) Raman spectrum taken from the LFP-rGO (Mg) composite. (d) Low magnification and (e) high magnification TEM images taken from the LFP-rGO (Mg) composite sample. (f) High resolution TEM image taken from the boundary of LFP particle. (g) HAADF image taken from part of this composite sample. (h)–(m) EDX elemental mapping taken from the same region shown in Fig. 4(g). (h) C; (i) Fe; (j) P; (k) O; and (l) Mg maps. (m) Overlap image of C, Fe, and Mg.

Fig. 4 shows the representative structural characterization results taken from the LFP-rGO (Mg) sample (similar to that taken from the LFP-rGO). SEM image in Fig. 4(a) shows the quasi-spherical LFP particles with an average size of ~280 nm (with size ranging from ~100 to 650 nm, Fig. S4, Supporting Information) being uniformly connected to or wrapped by thin sheet-like layers of rGO. The EDX taken from the same sample confirms that it is mainly composed of C, Fe, P, and O with trace amount of Mg (Fig. S3(b), Supporting Information). The crystallinity of LFP after the composite formation (92.50%, Fig. 4(b)) is found to be the same as that of the pristine LFP powders (93.26%, Fig. 1(c)). All Bragg peaks in the XRD data taken from LFP-rGO (Mg) can be indexed to the orthorhombic LFP phase. No obvious reflection from rGO is observed due to its very low content in the composite. The structure details of the rGO in the composite sample are examined by Raman spectroscopy. The Raman spectrum in Fig. 4(c) reveals the degree of graphitization of carbon in the LFP-rGO (Mg) composite. The D band at 1344 cm^{-1} is attributed to defects and disordered portions of carbon (sp^3) [25]. The G band at 1594 cm^{-1} is indicative of ordered graphitic crystallites of carbon (sp^2) [25]. The I_D/I_G ratio of LFP-rGO (Mg) is 0.72. The change of the I_D/I_G ratio as compared to the samples without rGO (LFP, 1.11; LFP (Mg), 1.03; Fig. S5, Supporting Information) is due to introduction of rGO, in which the sp^2 coordinated carbon dominates [12]. The content of rGO in this LFP-rGO (Mg) composite is ~7.2 wt%, which is estimated using TGA (Fig. S6, Supporting Information). According to BET analysis, the specific surface area of LFP-rGO (Mg) is 34.1 $m^2\ g^{-1}$. The specific surface area of LFP-rGO (Mg) is higher than that of LFP (Mg) (15.3 $m^2\ g^{-1}$), which is attributed to the large surface area of rGO. On the other hand, the specific surface area of LFP-rGO (33.2 $m^2\ g^{-1}$) is close to that of LFP-rGO (Mg), suggesting that the presence of Mg^{2+} in the LFP-rGO leads to little change of surface areas.

More detailed structural characterization of the LFP-rGO (Mg) composite sample is carried out using TEM. Fig. 4(d) and (e) suggest that LFP nanoparticles are anchored on the rGO nanosheets. An amorphous carbon layer of ~3–4 nm is observed on the LFP surface (Fig. 4(f)), coming from the original carbon coating in the pristine LFP powders (Fig. 1(c)). In addition, spatial distribution of the compositional elements is disclosed by EDX elemental mapping (Fig. 4(g) and (m)), revealing the uniform distribution of the compositional elements.

Fig. 5(a)–(c) show the typical O 1s, P 2p, and Fe 2p spectra taken from the LFP-rGO and the LFP-rGO (Mg) samples. The Mg 1s spectrum of LFP-rGO (Mg) is shown in Fig. S7 (Supporting Information). Fitting of the O 1s, P 2p, and Fe 2p XPS show similar origin as those in the previous LFP and LFP (Mg) samples. When compared to LFP-rGO, the peak of O 1s spectrum of LFP-rGO (Mg) composite is found to shift toward higher binding energy (Fig. 5(a)). Furthermore, fitting of the O 1s XPS spectra shows the peak of P-O located at around 531.45 eV in LFP-rGO, while it is blue-shifted to 531.78 eV in LFP-rGO (Mg). Meanwhile, the Fe-O peak area of the LFP-rGO

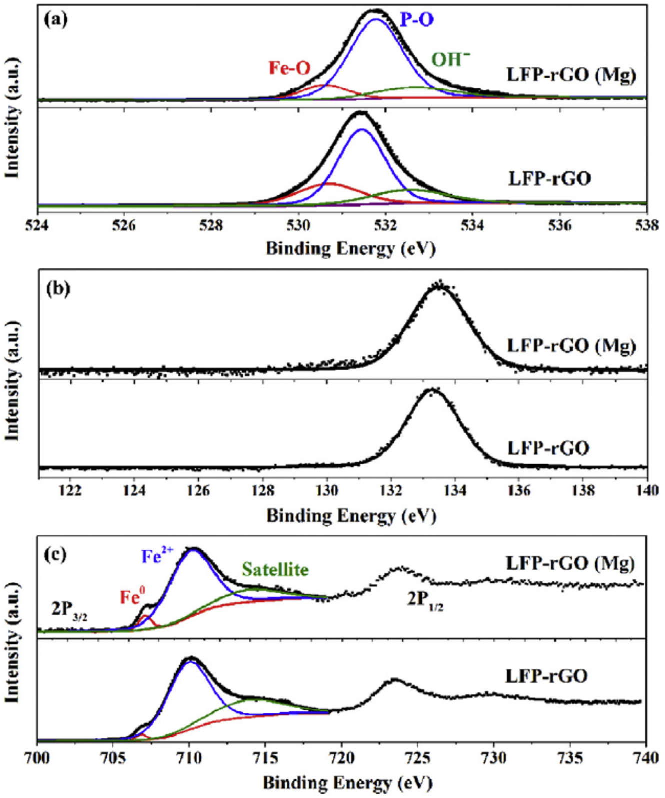

Fig. 5. (a) O 1s, (b) P 2p, and (c) Fe 2p XPS spectra of the LFP-rGO and LFP-rGO (Mg).

(Mg) is decreased when compared to that of the LFP-rGO. Fig. 5(b) shows the P 2p peak located at 133.30 eV in the spectrum of LFP-rGO, and it is blue-shifted to 133.50 eV in that of LFP-rGO (Mg). In Fe 2p XPS spectrum of LFP-rGO (Mg), although no peak shifting is observed, the peak representing metallic iron becomes more obvious when compared to that of LFP-rGO. The area ratios of Fe^0 are estimated to be ~1.7% and ~5.0% in the Fe $2p_{3/2}$ spectrum of LFP-rGO and LFP-rGO (Mg), respectively. The above experimental results suggest a decrease of Fe^{2+}, and an increase of Fe^0 when Mg^{2+} is introduced to the LFP-rGO. The enhanced reduction of Fe^{2+} to Fe^0 in LFP is consistent with the blue shifts observed in both the O 1s peak and the P 2p peak in the LFP-rGO (Mg) sample relatively to those in the LFP-rGO sample. In fact, the blue shift observed in the O 1s spectrum in such a sample also excludes the possibility of Mg doping into the LFP lattice (i.e., Mg^{2+} taking the substitutional site of Fe^{2+}), which would then cause red-shift in O 1s peak instead of blue shift [26]. Moreover, XRD and Rietveld refinement data (Fig. S8 and Table S2, Supporting Information) demonstrate that the presence of Mg^{2+} in the LFP or LFP-rGO leads to little change in the lattice parameters of LFP. This further excludes the possibility of Mg^{2+} substituting for Fe^{2+}.

Coin cells are assembled using LFP-rGO or LFP-rGO (Mg) as the active materials, and their electrochemical properties are evaluated. The first charging and discharging profiles of the respective samples cycled at 0.1 C are shown in Fig. 6(a). The average plateau is observed around 3.42 V vs. Li^+/Li. The polarization between the charging and discharging plateau for the LFP-rGO (Mg) sample is ~60 mV, being smaller than that of the LFP-rGO sample (~71 mV). This indicates the LFP-rGO (Mg) has lower internal resistance. These cells are tested under various charging/discharging rates and their specific capacities are shown in Fig. 6(b). At low charging/

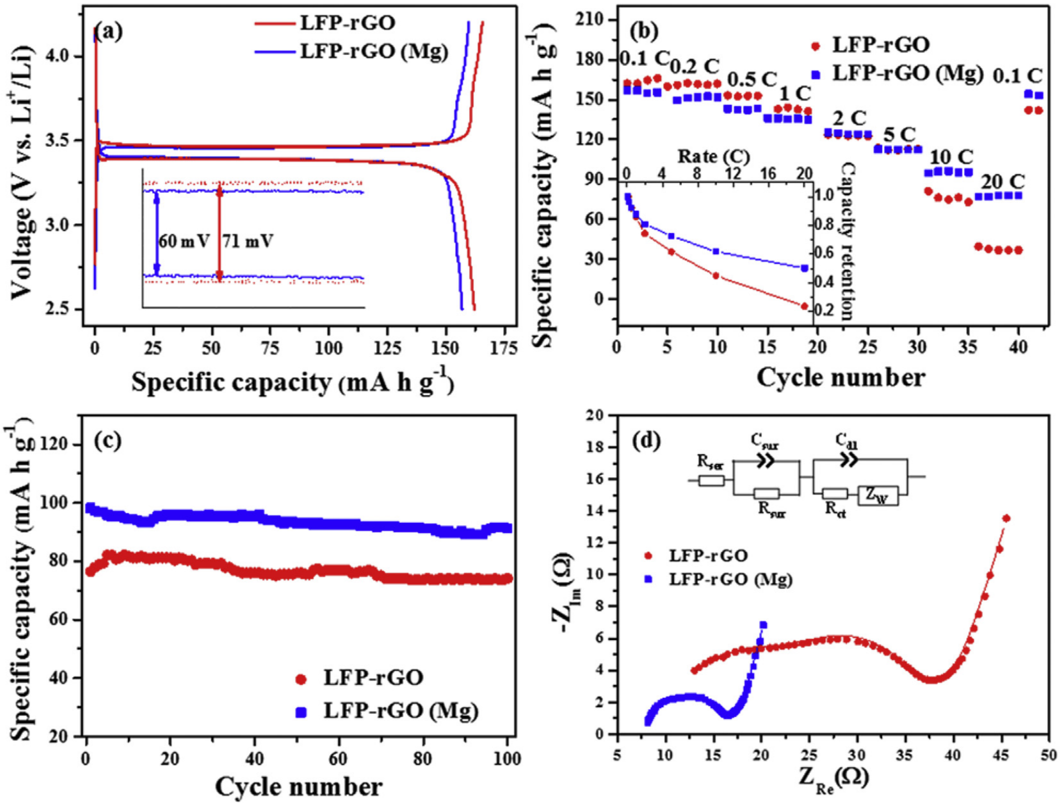

Fig. 6. (a) Comparison of the first charging and discharging profiles of LFP-rGO (Mg) and LFP-rGO samples at a rate of 0.1 C. (b) Specific capacities of the samples at various rates. Comparison of the specific capacity retention of the samples is shown in the inset. (c) Cycling stability of the samples cycled at a rate of 10 C. (d) Nyquist plots of the electrodes after charging the samples to ~4.2 V vs. Li^+/Li.

discharging rates (<1 C), the specific capacities of the LFP-rGO and the LFP-rGO (Mg) samples are rather close. However, the LFP-rGO (Mg) sample shows much higher specific capacities at high charging/discharging rates (e.g. 10 and 20 C), suggesting superior rate performance, which is obvious when one compares the capacity retention of these electrodes (inset in Fig. 6(b)). Despite the higher capacity of the LFP-rGO (Mg) at high rates, the cycling performances of both samples are good (Fig. 6(c)).

The Nyquist plots are shown in Fig. 6(d). An appropriate equivalent circuit model (inset in Fig. 6(d)) is established to fit the Nyquist curves. The electrical parameters (e.g., R_{ser}, R_{sur}, and R_{ct}) in this model can be calculated, as shown in Table S3 (Supporting Information). Both the charge transfer resistance R_{ct} and the SEI layer resistance R_{sur} of the LFP-rGO (Mg) electrode decreases significantly. Consequently, the decreased charge transfer resistance and surface layer resistance in the LFP-rGO (Mg) electrode lead to the smaller polarization as compared to the LFP-rGO electrode (Fig. 6(a)), resulting in much better rate performance observed in the LFP-rGO (Mg) electrode (Fig. 6(b)). To examine the effect of adding Mg^{2+} on the Li^{+} transport properties, the effective Li^{+} diffusion coefficient D_{Li} is estimated from the EIS data. The estimated values of the D_{Li} are ~2.35 × 10^{-10} and ~5.28 × 10^{-10} cm^2 s^{-1} for LFP-rGO, and LFP-rGO (Mg) samples, respectively, suggesting little effect of Mg^{2+} presence on the Li^{+} diffusion in the LFP-rGO composite samples.

The introduction of rGO in LFP-based electrodes improves the electrochemical properties of the cathode, including both higher specific capacity and slightly higher rate capacity retention at high rates (Fig. S9, Supporting Information). This should be ascribed to the formation of conductive pathways for electron transport during the charging/discharging process, as evidenced in decreased charge transfer resistance (Tables S1 and S3, Supporting Information). In addition, it is known that rGO can deliver a specific capacity of ~64 mA h g^{-1} [7]. Therefore, the rGO may contribute an extra capacity of ~4 mA h g^{-1} to the composite samples (as compared to the LFP) by considering the weight percentage of rGO in the present LFP-rGO composite electrode (~7 wt%).

A significant improvement in the rate performance of the cathode is observed when Mg^{2+} is further introduced to the LFP/rGO composite (Fig. 6(b)). The charging and discharging profiles as well as EIS data indicate that introduction of Mg^{2+} into the LFP/rGO composite leads to significantly enhanced electronic conductivity, likely due to generation of more Fe^0 in the LFP-rGO (Mg) sample. The presence of conductive metallic phases is known to improve the conductivity of LFP [27]. It is interesting to note that the increase of Fe amount prompted by Mg^{2+} only takes place in the presence of rGO. This result suggests possible influence of reaction kinetic barriers during the carbothermal reduction of Fe^{2+} to Fe^0—the simultaneous presence of Mg^{2+} and rGO promotes such reduction. Moreover, experimental results also suggest that no Fe^0 exists in the composites before annealing and the enhanced reduction of Fe^{2+} to Fe^0 in LFP occurs during the annealing process (Figs. S10–12, Supporting Information).

The electrochemical properties of LFP/rGO composite are fairly sensitive to the amount of Mg^{2+}. The optimum Mg^{2+} amount has been identified during the composite cathode fabrication and the results are presented in Fig. S13 (Supporting Information). The Mg^{2+} element content is varied at different LFP/Mg mass ratio (260:1, 130:1, and 78:1) and the rGO content is maintained at ~7 wt % in a series of electrode samples, i.e., LFP-rGO (Mg)_1, LFP-rGO (Mg)_2, and LFP-rGO (Mg)_3. These cells are tested under various charging/discharging rates and their specific capacities are shown in Fig. S13(a) (Supporting Information). Compared to the LFP-rGO sample, higher specific capacities at high charging/discharging rates (10 and 20 C) are always observed in the presence of Mg^{2+}. The LFP-rGO (Mg)_2 sample exhibits the highest specific capacities at high rates among all samples, suggesting its superior rate performance (Fig. S13(b), Supporting Information). The Nyquist plots and corresponding fitting parameters (e.g., R_{ser}, R_{sur}, R_{ct}, and D_{Li}) are shown in Fig. S13(c) and Fig. S13(d) (Supporting Information), respectively. Observable difference of the charge transfer resistance R_{ct} is detected in the LFP/rGO composite with different Mg^{2+} amount. At lower Mg^{2+} amount, (e.g. LFP/Mg mass ratio 260:1 and 130:1), decreased R_{ct} is observed with Mg^{2+} incorporation. At higher Mg^{2+} amount (e.g. LFP/Mg mass ratio 78:1), the effect of Mg^{2+} hydrolysis becomes dominant, leading to $Mg(OH)_2$ formation that is detrimental to the electronic conductivity of composite [12]. The estimated values of the D_{Li} are ~2.92 × 10^{-10}, ~5.28 × 10^{-10} and ~3.6 × 10^{-10} cm^2 s^{-1} for LFP-rGO (Mg)_1, LFP-rGO (Mg)_2, and LFP-rGO (Mg)_3. They are in the same order of magnitude. Different amount of Mg^{2+} incorporation does not significantly affect the Li^{+} diffusion in these samples.

4. Conclusions

We found adding Mg^{2+} only into LFP followed by annealing lead to obvious change in neither the electronic structure nor the electrochemical properties of LFP cathode. On the other hand, introducing rGO to LFP cathode results in moderately increased specific capacity at high rates. Further adding Mg^{2+} into LFP cathode with the presence of rGO brings significantly improved rate performance. Experimental evidence suggests that enhanced reduction of Fe^{2+} to Fe^0 prompted by Mg^{2+} and rGO leads to the improvement electronic conductivity of the LFP/rGO composite electrode. The simple fabrication process does not disturb the active material growth process and it provides a simple and effective means to improve the rate performance of the LFP/rGO composite.

Acknowledgements

This work is supported by General Research Funding of the National Natural Science Foundation of China/Research Grants Council Joint Research Scheme under project No. N_CUHK448/13.

Appendix A. Supplementary data

Supplementary data related to this article can be found at http://dx.doi.org/10.1016/j.jpowsour.2017.02.043.

References

[1] Z. Li, Z. Peng, H. Zhang, T. Hu, M. Hu, K. Zhu, X. Wang, [100]-Oriented $LiFePO_4$ nanoflakes toward high rate Li-ion battery cathode, Nano Lett. 16 (2016) 795–799.

[2] K. Zhang, J.-T. Lee, P. Li, B. Kang, J.H. Kim, G.-R. Yi, J.H. Park, Conformal coating strategy comprising N-doped carbon and conventional graphene for achieving ultrahigh power and cyclability of $LiFePO_4$, Nano Lett. 15 (2015) 6756–6763.

[3] Y. Zhang, H.J. Zhang, Y.Y. Feng, L. Fang, Y. Wang, Ultralong lifespan and ultrafast Li storage: single crystal $LiFePO_4$ nanomeshes, Small 12 (2016) 516–523.

[4] Z. Ma, Y. Fan, G. Shao, G. Wang, J. Song, T. Liu, In situ catalytic synthesis of high-graphitized carbon-coated $LiFePO_4$ nanoplates for superior Li-ion battery cathodes, ACS Appl. Mater. Interfaces 7 (2015) 2937–2943.

[5] J. Wang, X. Sun, Understanding and recent development of carbon coating on $LiFePO_4$ cathode materials for lithium-ion batteries, Energy Environ. Sci. 5 (2012) 5163–5185.

[6] P.S. Herle, B. Ellis, N. Coombs, L.F. Nazar, Nano-network electronic conduction in iron and nickel olivine phosphates, Nat. Mater. 3 (2004) 147–152.

[7] B. Wang, B. Xu, T. Liu, P. Liu, C. Guo, S. Wang, Q. Wang, Z. Xiong, D. Wang, X.S. Zhao, Mesoporous carbon-coated $LiFePO_4$ nanocrystals co-modified with graphene and Mg^{2+} doping as superior cathode materials for lithium ion batteries, Nanoscale 6 (2014) 986–995.

[8] Z. Yang, J. Xia, L. Zhi, W. Zhang, B. Pei, An improved solid-state reaction route to Mg^{2+}-doped $LiFePO_4$/C cathode material for Li-ion battery, Ionics 20 (2014) 169–174.

[9] S. Ferrari, R.L. Lavall, D. Capsoni, E. Quartarone, A. Magistris, P. Mustarelli, P. Canton, Influence of particle size and crystal orientation on the electrochemical behavior of carbon-coated $LiFePO_4$, J. Phys. Chem. C 114 (2010) 12598–12603.

[10] J. Ha, S.-K. Park, S.-H. Yu, A. Jin, B. Jang, S. Bong, I. Kim, Y.-E. Sung, Y. Piao, A chemically activated graphene-encapsulated $LiFePO_4$ composite for high-performance lithium ion batteries, Nanoscale 5 (2013) 8647–8655.

[11] Y. Long, Y. Shu, X. Ma, M. Ye, In-situ synthesizing superior high-rate $LiFePO_4$/C nanorods embedded in graphene matrix, Electrochim. Acta 117 (2014) 105–112.

[12] Y. Huang, H. Liu, Y.C. Lu, Y. Hou, Q. Li, Electrophoretic lithium iron phosphate/reduced graphene oxide composite for lithium ion battery cathode application, J. Power Sources 284 (2015) 236–244.

[13] H. Zhang, Y. Tang, J. Shen, X. Xin, L. Cui, L. Chen, C. Ouyang, S. Shi, L. Chen, Antisite defects and Mg doping in $LiFePO_4$: a first-principles investigation, Appl. Phys. A 104 (2011) 529–537.

[14] W.S. Hummers, R.E. Offeman, Preparation of graphitic oxide, J. Am. Chem. Soc. 80 (1958), 1339–1339.

[15] A.F. Orliukas, K.-Z. Fung, V. Venckutė, V. Kazlauskienė, J. Miškinis, A. Dindune, Z. Kanepe, J. Ronis, A. Maneikis, T. Šalkus, A. Kežionis, SEM/EDX, XPS, and impedance spectroscopy of $LiFePO_4$ and $LiFePO_4$/C ceramics, Lith. J. Phys. 54 (2014) 106–113.

[16] S. Praneetha, A.V. Murugan, A rapid, one-pot microwave-solvothermal synthesis of a hierarchical nanostructured graphene/$LiFePO_4$ hybrid as a high performance cathode for lithium ion batteries, RSC Adv. 3 (2013) 25403–25409.

[17] Y. Zheng, Y.-B. He, K. Qian, B. Li, X. Wang, J. Li, C. Miao, F. Kang, Effects of state of charge on the degradation of $LiFePO_4$/graphite batteries during accelerated storage test, J. Alloys Compd. 639 (2015) 406–414.

[18] J. Weissenrieder, M. Göthelid, M. Månsson, H. von Schenck, O. Tjernberg, U.O. Karlsson, Oxygen structures on Fe(110), Surf. Sci. 527 (2003) 163–172.

[19] X. Jiang, J. Qiao, I.M.C. Lo, L. Wang, X. Guan, Z. Lu, G. Zhou, C. Xu, Enhanced paramagnetic Cu^{2+} ions removal by coupling a weak magnetic field with zero valent iron, J. Hazard. Mater. 283 (2015) 880–887.

[20] A. Bünting, S. Uhlenbruck, D. Sebold, H.P. Buchkremer, R. Vaßen, Three-dimensional, fibrous lithium iron phosphate structures deposited by magnetron sputtering, ACS Appl. Mater. Interfaces 7 (2015) 22594–22600.

[21] L. Castro, R. Dedryvère, M. El Khalifi, P.-E. Lippens, J. Bréger, C. Tessier, D. Gonbeau, The spin-polarized electronic structure of $LiFePO_4$ and $FePO_4$ evidenced by in-lab XPS, J. Phys. Chem. C 114 (2010) 17995–18000.

[22] D. Cíntora-Juárez, C. Pérez-Vicente, S. Kazim, S. Ahmad, J.L. Tirado, Judicious design of lithium iron phosphate electrodes using poly(3,4-ethylenedioxythiophene) for high performance batteries, J. Mater. Chem. A 3 (2015) 14254–14262.

[23] J. Li, Y. Jiang, G. Bai, T. Ma, D. Yang, Y. Du, M. Yan, Room temperature ferromagnetism of amorphous MgO films prepared by pulsed laser deposition, Appl. Phys. A 115 (2014) 997–1001.

[24] E. Barsoukov, J.R. Macdonald, Impedance Spectroscopy: Theory, Experiment, and Applications, second ed., Wiley, Hoboken, NJ, 2005.

[25] K.N. Kudin, B. Ozbas, H.C. Schniepp, R.K. Prud'homme, I.A. Aksay, R. Car, Raman spectra of graphite oxide and functionalized graphene sheets, Nano Lett. 8 (2008) 36–41.

[26] D. Wang, H. Li, S. Shi, X. Huang, L. Chen, Improving the rate performance of $LiFePO_4$ by Fe-site doping, Electrochim. Acta 50 (2005) 2955–2958.

[27] G.-M. Songa, Y. Wu, Q. Xu, G. Liu, Enhanced electrochemical properties of $LiFePO_4$ cathode for Li-ion batteries with amorphous NiP coating, J. Power Sources 195 (2010) 3913–3917.